Progress In Electromagnetics Research, PIER 44, 1–38, 2004

A FAST MULTIPOLE METHOD FOR EMBEDDED STRUCTURE IN A STRATIFIED MEDIUM

Y. C. Pan

Logic Technology Development
Microprocessor Design Group
Intel Corporation
Hillsboro, OR 97124-6461, USA

W. C. Chew

Center for Computational Electromagnetics
and Electromagnetics Laboratory
Department of Electrical and Computer Engineering
University of Illinois
Urbana, IL 61801-2991, USA

Abstract—An efficient, static fast multipole method (FMM) based algorithm is presented in this paper for the evaluation of the parasitic capacitance of 3-D microstrip signal lines embedded in stratified dielectric media. The effect of dielectric interfaces on the capacitance matrix is included in the stage of FMM when outgoing multipole expansions are used to form local multipole expansions. The algorithm retains $O(N)$ computational and memory complexity of the free-space FMM, where N is the number of conductor patches.

1. INTRODUCTION

Characterization of VLSI circuit layouts has become a vital part of the semiconductor design process. In a VLSI circuit, the conductor transmission lines are embedded in multiple layers of dielectrics. A considerable amount of research have been devoted to extracting the capacitance matrices of such multiconductor structures [1–7]. The most common approach to solving this type of capacitance problems, which involves arbitrarily shaped three-dimensional conductors embedded in multilayered dielectrics, is the integral-equation method. The unknowns in the integral-equation method are the charge densities on the surfaces of conductors and dielectrics. The method of moments (MOM) [8] is used to solve the integral equation by expanding the charge densities with a set

of basis functions and reducing the integral equation to a dense matrix equation. The limitation to seeking a numerical solution to this dense matrix equation is the number of unknowns in the problem. Let N be the number of unknowns. Solving a dense $N \times N$ matrix equation by direct inversion requires $O(N^3)$ operations, which can easily exhaust computational resources with a moderately-sized problem. The computational complexity can be reduced to $O(N^2)$ per iteration using an iterative solver. The fast multipole method (FMM), first proposed by Greengard and Rokhlin [9] to evaluate potentials in an N-particle system in free space, can further reduce this cost to $O(N)$ per iteration.

The free-space FMM is a divide-and-conquer technique that reduces the cost of solving Laplace's equation by separating sources into near and distant groups. Contributions from sources in near groups are computed directly, while contributions from sources in distant groups are added by first translating the outgoing multipole expansions of these groups to a local expansion, and then evaluating the local expansion. The translation is done by the outgoing-to-local (O2L) multipole translation matrix. Detailed descriptions of this algorithm can be found in [9, 10], and [11]. Successful implementation of the free-space FMM can reduce the computational complexity and memory requirement of a matrix-vector multiplication from $O(N^2)$ to $O(N)$.

Numerous attempts have been made to extend the free-space FMM to a stratified dielectric medium [12–14]. The motivation behind this research is that an efficient stratified medium FMM (SMFMM) can greatly reduce the cost of extracting parasitics in VLSI designs. Recently, we proposed an efficient SMFMM algorithm for conductors above stratified media [15, 16]. The key idea behind our development is the image outgoing multipole expansion. The image outgoing multipole expansion is the expansion of the image charges with respect to the center of the image cube. As we have shown in [15] and [16], the image outgoing multipole expansions can be deduced directly from the free-space outgoing multipole expansions. This idea enabled us to safely ignore the image sources and work directly with the image outgoing multipole expansions. In our algorithms, the effect of stratified media is incorporated by translating the image outgoing multipole expansions to the observation cube in the disaggregation stage of the FMM.

The objective of this paper is to extend our previous method to the general case of conductors embedded in the stratified dielectric media (see Figure 1). In Section 1, the multilayer Green's function is derived. The multilayer Green's function is needed because the

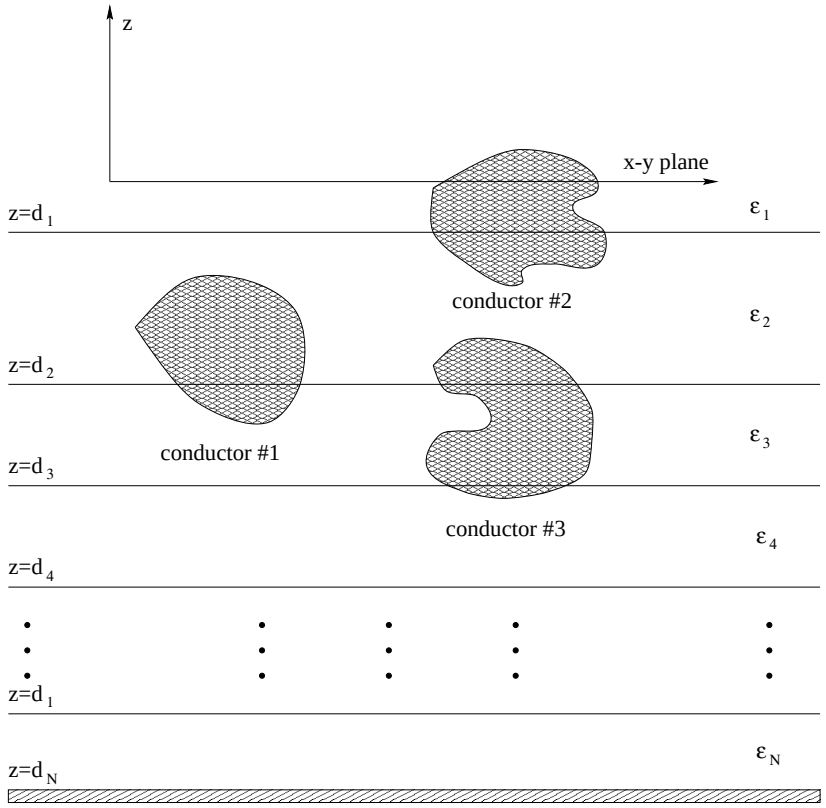

Figure 1. Multiple conductors embedded in a stratified dielectric medium.

sources in the near groups require direct computation. In Section 2, the O2L multipole translator for a stratified medium is formulated. The formulas are verified against published results. The new SMFMM algorithm is presented in Section 3, followed by numerical examples in Section 4.

2. STRATIFIED MEDIUM GREEN'S FUNCTION

2.1. Integral Representation of the Spherical Harmonics

The integral representation of the spherical harmonics is the basis for the derivation of our multilayer Green's function and O2L multipole translators. In this section, we will review these well-known

representations. The monopole $1/r$ has an integral representation of

$$\frac{1}{r} = \int_0^\infty J_0(\lambda\rho)e^{-\lambda|z|}d\lambda \tag{1}$$

where $\rho = \sqrt{x^2+y^2}$ and $J_0(\lambda\rho)$ is the zeroth-order Bessel function. For $z \simeq 0$, the integral converges slowly. This problem can be solved by deforming the contour of integration and writing

$$\frac{1}{r} = \frac{1}{\pi}\int_0^\infty K_0(\lambda\rho)\left[e^{i\lambda z} + e^{-i\lambda z}\right]d\lambda. \tag{2}$$

Here $K_0(\lambda\rho)$ is the zeroth-order modified Bessel function. The two exponential functions in parentheses sum to $2\cos(\lambda\rho)$. However, we keep these exponential terms separated because they cannot be combined in a multilayer Green's function.

In general, the integral representation of the spherical harmonics $Y_{nm}(\theta,\phi)/r^{n+1}$ is

$$\frac{Y_{nm}(\theta,\phi)}{r^{n+1}} = \begin{cases} \dfrac{(-1)^n e^{im\phi}}{\sqrt{(n-m)!(n+m)!}}\displaystyle\int_0^\infty \lambda^n J_{|m|}(\lambda\rho)e^{\lambda z}d\lambda & z \le 0 \\ \dfrac{(-1)^m e^{im\phi}}{\sqrt{(n-m)!(n+m)!}}\displaystyle\int_0^\infty \lambda^n J_{|m|}(\lambda\rho)e^{-\lambda z}d\lambda & z \ge 0 \end{cases} \tag{3}$$

Similarly, when $z \simeq 0$

$$\frac{Y_{nm}(\theta,\phi)}{r^n+1} = \frac{(-1)^n i^{n-|m|}e^{im\phi}}{\pi\sqrt{(n-m)!(n+m)!}}\int_0^\infty \lambda^n K_m(\lambda\rho)\left[e^{i\lambda z} + (-1)^{n-m}e^{-i\lambda z}\right]d\lambda \tag{4}$$

In Figure 2, the absolute errors of numerically integrating Equations (3) and (4) are plotted against the zenith angle θ.

The integrands in Equations (2) and (4) are singular at $\lambda = 0$ due to the modified Bessel function $K_m(\lambda\rho)$. The singularities, fortunately, are integrable because

$$\lim_{\lambda\rho\to 0} K_0(\lambda\rho) = \ln(\lambda\rho) \tag{5}$$

and for $|m| > 0$,

$$\lim_{\lambda\rho\to 0} \lambda^n K_m(\lambda\rho) = \frac{\Gamma(|m|)}{2}\lambda^n\left(\frac{\lambda\rho}{2}\right)^{-|m|}. \tag{6}$$

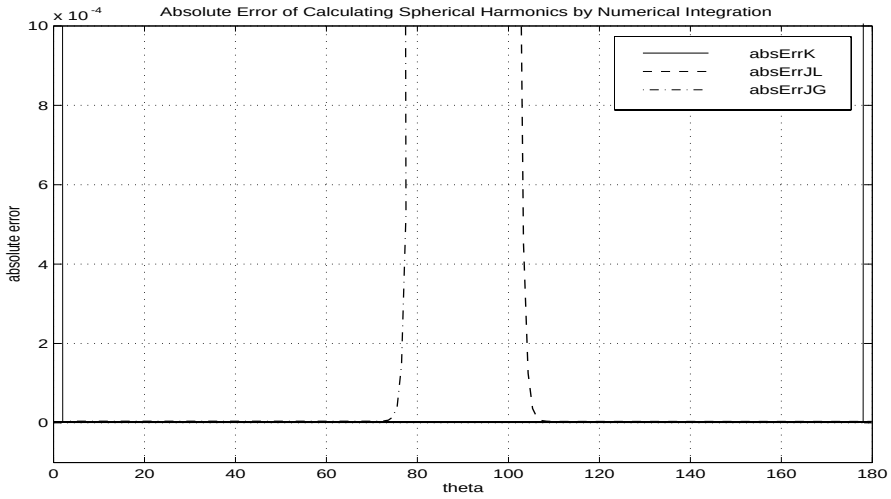

Figure 2. The absolute errors of numerically integrating Equations (3) and (4). The distance $r = 1.5$ and the azimuthal angle $\phi = 72°$. The order of spherical harmonics is $n = 2,\ m = 1$.

2.2. Integral Representation of the Stratified Medium Green's Function

In general, if the source and observation points are both within the region bounded above by d_{U-1} and below by d_L, the images can be separated into four sets. The locations of the first image of each set are specified in Figure 3. The effect of one set of images can be represented by one of the following integrals:

$$\tilde{G}(\delta\mathbf{r}) = \begin{cases} \displaystyle\int_0^\infty d\lambda J_0(\lambda\rho) e^{\lambda Z} \Omega(\lambda) & Z \leq 0 \\ \displaystyle\int_0^\infty d\lambda J_0(\lambda\rho) e^{-\lambda Z} \Omega(\lambda) & Z \geq 0 \end{cases} \tag{7}$$

or if $Z \simeq 0$

$$\tilde{G}(\delta\mathbf{r}) = \frac{1}{\pi} \int_0^\infty d\lambda K_0(\lambda\rho) \left[e^{-i\lambda|Z|} \Omega(i\lambda) + e^{i\lambda|Z|} \Omega(-i\lambda) \right]. \tag{8}$$

Here Z is the difference between the z-coordinates of the first set of images and the observation point.

When the source and the observation points are both in the same

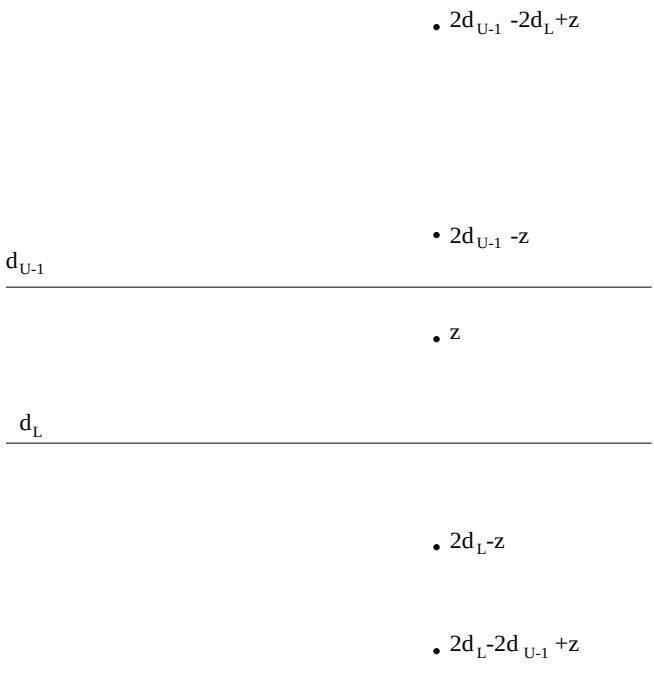

Figure 3. The locations of the first set of images of a source point in a stratified medium. The observation point is also in the region bounded by d_{U-1} and d_L.

layer of a multilayered medium, the Green's function has the form

$$\begin{aligned} G(\mathbf{r},\mathbf{r}') = G_0(\mathbf{r},\mathbf{r}') + \tilde{G}_{LL}^{MM}(\mathbf{r},\mathbf{r}_{LL}^{MM}) + \tilde{G}_{LU}^{MM}(\mathbf{r},\mathbf{r}_{LU}^{MM}) \\ + \tilde{G}_{UL}^{MM}(\mathbf{r},\mathbf{r}_{UL}^{MM}) + \tilde{G}_{UU}^{MM}(\mathbf{r},\mathbf{r}_{UU}^{MM}) \end{aligned} \tag{9}$$

where

$$G_0(\mathbf{r},\mathbf{r}') = \frac{1}{|\mathbf{r}-\mathbf{r}'|} \tag{10}$$

is the free-space Green's function. The weighting functions for the four image terms are

$$\Omega_{LL}^{MM}(\lambda) = \frac{\tilde{R}_{M,M+1}(\lambda)\tilde{R}_{M,M-1}(\lambda)}{1-\tilde{R}_{M,M+1}(\lambda)\tilde{R}_{M,M-1}(\lambda)e^{-\lambda 2t_M}} \tag{11}$$

$$\Omega_{LU}^{MM}(\lambda) = \frac{\tilde{R}_{M,M+1}(\lambda)}{1-\tilde{R}_{M,M+1}(\lambda)\tilde{R}_{M,M-1}(\lambda)e^{-\lambda 2t_M}} \tag{12}$$

$$\Omega_{UL}^{MM}(\lambda) = \frac{\tilde{R}_{M,M-1}(\lambda)}{1 - \tilde{R}_{M,M+1}(\lambda)\tilde{R}_{M,M-1}(\lambda)e^{-\lambda 2t_M}} \tag{13}$$

$$\Omega_{UU}^{MM}(\lambda) = \frac{\tilde{R}_{M,M+1}(\lambda)\tilde{R}_{M,M-1}(\lambda)}{1 - \tilde{R}_{M,M+1}(\lambda)\tilde{R}_{M,M-1}(\lambda)e^{-\lambda 2t_M}} \tag{14}$$

and the differences between the z-coordinates of the first of each set of images and the observation point are

$$\begin{aligned} Z_{LL}^{MM} &= -2t_M + z' - z \\ Z_{LU}^{MM} &= 2d_M - z' - z \\ Z_{UL}^{MM} &= 2d_{M-1} - z' - z \\ Z_{UU}^{MM} &= 2t_M + z' - z. \end{aligned} \tag{15}$$

In Equations (11)–(14), M is the layer number and $\tilde{R}_{i,i\pm1}(\lambda)$ are the generalized reflection coefficients. It should be noted here that Equation (10) can be combined with either Equation (11) or (14), depending on the relative z-coordinate of the source point with respect to the z-coordinate of the observation point. For fast convergence of numerical integrations, however, it is advantageous to keep the free-space term separated.

Table 1. Comparison of numerically integrated Green's function with data published in [18]. The source and observation points are in the same dielectric region. In all cases, it is assumed that $z' = z = 0$.

	ϵ_{r1}=9.80 h_1=1.0 mm ϵ_{r2}=2.55 h_2=1.0 mm			ϵ_{r1}=2.55 h_1=1.0 mm ϵ_{r2}=9.80 h_2=1.0 mm		
ρ(mm)	NI [18]	CI [18]	NI, MM	NI [18]	CI [18]	NI, MM
0.1	1623.00	1622.12	1622.29	1521.93	1522.00	1522.03
0.6	270.69	270.20	270.20	176.94	176.99	177.00
1.1	142.92	142.91	142.91	63.23	63.22	63.23
1.6	91.68	91.90	91.90	27.55	27.53	27.53
2.1	63.30	63.52	63.52	13.17	13.15	13.16
3.1	33.22	33.31	33.31	3.58	3.58	3.59

The validity of Equation (9) is checked by comparing with the numerical values in Table IV of [18]. The results are found in Table 1. In Table 1, columns marked by NI and CI are numerical values taken from [18], and columns marked by MM are calculated with Equation (9).

Let M be the region containing the source point, and N be the region containing the observation point.

If region M is above region N, then the Green's function has the form

$$\begin{aligned} G(\mathbf{r},\mathbf{r}') = \tilde{G}_{LL}^{MN}(\mathbf{r},\mathbf{r}_{LL}^{MN}) + \tilde{G}_{LU}^{MN}(\mathbf{r},\mathbf{r}_{LU}^{MN}) \\ + \tilde{G}_{UL}^{MN}(\mathbf{r},\mathbf{r}_{UL}^{MN}) + \tilde{G}_{UU}^{MN}(\mathbf{r},\mathbf{r}_{UU}^{MN}). \end{aligned} \tag{16}$$

The weighting functions for the four image terms are

$$\Omega_{LL}^{MN}(\lambda) = \frac{\tilde{T}_{M,N}^{-}(\lambda)\tilde{R}_{N,N+1}(\lambda)\tilde{R}_{M,M-1}(\lambda)}{1-\tilde{R}_{M,M+1}(\lambda)\tilde{R}_{M,M-1}(\lambda)e^{-\lambda 2t_M}} \tag{17}$$

$$\Omega_{LU}^{MN}(\lambda) = \frac{\tilde{T}_{M,N}^{-}(\lambda)\tilde{R}_{N,N+1}(\lambda)}{1-\tilde{R}_{M,M+1}(\lambda)\tilde{R}_{M,M-1}(\lambda)e^{-\lambda 2t_M}} \tag{18}$$

$$\Omega_{UL}^{MN}(\lambda) = \frac{\tilde{T}_{M,N}^{-}(\lambda)}{1-\tilde{R}_{M,M+1}(\lambda)\tilde{R}_{M,M-1}(\lambda)e^{-\lambda 2t_M}} \tag{19}$$

$$\Omega_{UU}^{MN}(\lambda) = \frac{\tilde{T}_{M,N}^{-}(\lambda)\tilde{R}_{M,M-1}(\lambda)}{1-\tilde{R}_{M,M+1}(\lambda)\tilde{R}_{M,M-1}(\lambda)e^{-\lambda 2t_M}} \tag{20}$$

and the differences between the z-coordinates of the first of each set of images and the observation point are

$$\begin{aligned} Z_{LL}^{MN} &= 2d_N - 2d_{M-1} + z' - z \\ Z_{LU}^{MN} &= 2d_N - z' - z \\ Z_{UL}^{MN} &= z' - z \\ Z_{UU}^{MN} &= 2d_{M-1} - z' - z. \end{aligned} \tag{21}$$

If region M is below region N, then the Green's function has the form

$$\begin{aligned} G(\mathbf{r},\mathbf{r}') = \tilde{G}_{LL}^{NM}(\mathbf{r},\mathbf{r}_{LL}^{NM}) + \tilde{G}_{LU}^{NM}(\mathbf{r},\mathbf{r}_{LU}^{NM}) \\ + \tilde{G}_{UL}^{NM}(\mathbf{r},\mathbf{r}_{UL}^{NM}) + \tilde{G}_{UU}^{NM}(\mathbf{r},\mathbf{r}_{UU}^{NM}). \end{aligned} \tag{22}$$

The weighting functions for the four image terms are

$$\Omega_{LL}^{NM}(\lambda) = \frac{\tilde{T}_{N,M}^{+}(\lambda)\tilde{R}_{M,M+1}(\lambda)}{1-\tilde{R}_{M,M+1}(\lambda)\tilde{R}_{M,M-1}(\lambda)e^{-\lambda 2t_M}} \tag{23}$$

$$\Omega_{LU}^{NM}(\lambda) = \frac{\tilde{T}_{N,M}^{+}(\lambda)}{1-\tilde{R}_{M,M+1}(\lambda)\tilde{R}_{M,M-1}(\lambda)e^{-\lambda 2t_M}} \tag{24}$$

Table 2. Comparison of numerically integrated Green's function using Equations (9), (16), and (22). Column marked MM is produced using Equation (9). Column marked MN is produced using Equation (16). Column marked NM is produced using Equation (22). In all cases, it is assumed that $z' = z = 0$.

	ϵ_{r2}=9.80 h_1=1.0 mm			ϵ_{r2}=2.55 h_1=1.0 mm		
	ϵ_{r3}=2.55 h_2=1.0 mm			ϵ_{r3}=9.80 h_2=1.0 mm		
ρ(mm)	MM	MN	NM	MM	MN	NM
0.1	1622.29	1622.43	1622.43	1522.03	1522.02	1522.02
0.6	270.20	270.20	270.20	177.00	176.99	179.99
1.1	142.91	142.91	142.91	63.23	63.23	63.23
1.6	91.90	91.90	91.90	27.53	27.53	27.53
2.1	63.52	63.52	63.52	13.16	13.15	13.15
3.1	33.31	33.31	33.31	3.59	3.58	3.58

$$\Omega_{UL}^{NM}(\lambda) = \frac{\tilde{T}_{N,M}^{+}(\lambda)\tilde{R}_{N,N-1}(\lambda)}{1 - \tilde{R}_{M,M+1}(\lambda)\tilde{R}_{M,M-1}(\lambda)e^{-\lambda 2t_M}} \tag{25}$$

$$\Omega_{UU}^{NM}(\lambda) = \frac{\tilde{T}_{N,M}^{+}(\lambda)\tilde{R}_{N,N-1}\tilde{R}_{M,M+1}(\lambda)}{1 - \tilde{R}_{M,M+1}(\lambda)\tilde{R}_{M,M-1}(\lambda)e^{-\lambda 2t_M}} \tag{26}$$

and the differences between the z-coordinates of the first of each set of image and the observation point are

$$\begin{aligned} Z_{LL}^{NM} &= 2d_M - z' - z \\ Z_{LU}^{NM} &= z' - z \\ Z_{UL}^{NM} &= 2d_{N-1} - z' - z \\ Z_{UU}^{NM} &= 2d_{N-1} - 2d_M + z' - z. \end{aligned} \tag{27}$$

In Equations (17)–(20) and (23)–(26), $\tilde{T}_{i,j}^{\pm}(\lambda)$ are the generalized transmission coefficients.

Verification of Equations (16) and (22) is not as straightforward as Equation (9) because of the lack of published results. However, they can be checked indirectly through the use of boundary conditions and the reciprocity theorem. We note that the source and observation points in Table 1 are at the boundary of dielectric regions 2 and 3. Because the voltage must be continuous across a dielectric interface, the numerical values should stay constant as we force either the source point or the observation point from region 2 into region 3. In Table 2, we can see that the boundary condition is satisfied. In Table 3, the validity of Equations (16) and (22) is further checked using the

reciprocity theorem. Six pairs of source and observation points were chosen, with each pair having a point in region 1 and a point in region 3. It can be seen from Table 3 that the solutions of the two equations are in good agreement.

Table 3. Comparison of numerically integrated Green's function using Equations (16) and (22). For the columns marked MN, $z' = 1.1\,\text{mm}$ and $z = 0.1\,\text{mm}$. For the columns marked NM, $z' = 0.1\,\text{mm}$ and $z = 1.1\,\text{mm}$.

	$\epsilon_{r2} = 9.80$ $\epsilon_{r3} = 2.55$	$h_1 = 1.0\,\text{mm}$ $h_2 = 1.0\,\text{mm}$	$\epsilon_{r2} = 2.55$ $\epsilon_{r3} = 9.80$	$h_1 = 1.0\,\text{mm}$ $h_2 = 1.0\,\text{mm}$
ρ (mm)	MN	NM	MN	NM
0.1	177.64	177.64	97.05	97.05
0.6	153.28	153.28	79.41	79.41
1.1	116.20	116.20	53.68	53.68
1.6	84.63	84.63	33.49	33.49
2.1	61.56	61.56	20.43	20.43
3.1	33.64	33.64	7.75	7.75

3. STRATIFIED MEDIUM O2L TRANSLATORS

3.1. Integral Representation of the Free-Space O2L Translators

The free-space outgoing-to-local multipole translator is given by

$$\alpha_{nm}^{jk}(\mathbf{r}) = (-1)^{n+(|k-m|-|k|-|m|)/2} \left(\frac{a}{r}\right)^{j+n+1} \sqrt{\binom{j-k+n+m}{n+m}\binom{j+k+n-m}{n-m}} Y_{j+n,m-k}(\theta,\phi) \tag{28}$$

where a is the side length of cubes at a given level. Substituting Equations (3) and (4) into Equation (28), we have

$$\alpha_{nm}^{jk}(\mathbf{r}) = \begin{cases} (-1)^j A_{mn}^{jk} e^{i(m-k)\phi} \displaystyle\int_0^\infty \lambda^{j+n} J_{|m-k|}(\lambda\rho) e^{\lambda z} d\lambda & z \le 0 \\ (-1)^{n+m-k} A_{mn}^{jk} e^{i(m-k)\phi} \displaystyle\int_0^\infty \lambda^{j+n} J_{|m-k|}(\lambda\rho) e^{-\lambda z} d\lambda & z \ge 0 \end{cases} \tag{29}$$

or when $z \simeq 0$,

$$\alpha_{nm}^{jk}(\mathbf{r}) = \frac{i^{3j+n-|m-k|}}{\pi} A_{mn}^{jk} e^{i(m-k)\phi} \left[I_1 + (-1)^{j+n-m+k} I_2 \right]$$
$$I_1 = \int_0^\infty d\lambda \lambda^{j+n} K_{m-k}(\lambda\rho) e^{i\lambda z} \tag{30}$$
$$I_2 = \int_0^\infty d\lambda \lambda^{j+n} K_{m-k}(\lambda\rho) e^{-i\lambda z}.$$

In Equations (29) and (30), the constant coefficient A_{nm}^{jk} is defined as

$$A_{nm}^{jk} = \frac{(-1)^{(|k-m|-|k|-|m|)/2} a^{j+n+1}}{\sqrt{(j+k)!(j-k)!(n+m)!(n-m)!}} \tag{31}$$

3.2. Integral Representation of the Multilayer O2L Translators

In [15] and [16], we have observed that the outgoing multipole expansion of an image source with respect to the its image cube center can be found directly from the outgoing multipole expansion of the source with respect to its cube center. Therefore, efficient FMM for stratified media can be developed by translating the image outgoing multipole expansion in the disaggregation stage of the algorithm. Translation of one set of image outgoing multipole expansions can be summed into one image O2L translator. These image O2L translators are derived in this section.

In general, the contribution of a set of images to the multilayer O2L translator can be expressed by one of following integrals:

$$\tilde{\Lambda}_L(\mathbf{r}, \mathbf{r}'; n, m, j, k) = (-1)^j A_{mn}^{jk} e^{i(m-k)\phi} \int_0^\infty d\lambda \lambda^{j+n} J_{|m-k|}(\lambda\rho) e^{\lambda Z} \Omega(\lambda) \tag{32}$$

$$\tilde{\Lambda}_U(\mathbf{r}, \mathbf{r}'; n, m, j, k) = (-1)^{n+m-k} A_{mn}^{jk} e^{i(m-k)\phi} \int_0^\infty d\lambda \lambda^{j+n} J_{|m-k|}(\lambda\rho) e^{-\lambda Z} \Omega(\lambda). \tag{33}$$

In Equations (32) and (33), the subscript L denotes lower sets of images, and the subscript U denotes upper sets of images. When the difference between the z-coordinates of the first image cube center and the observation cube center is small, $Z \simeq 0$, the following equations

have better convergence:

$$\tilde{\Lambda}_L(\mathbf{r},\mathbf{r}';n,m,j,k) = \frac{i^{3j+n-|m-k|}}{\pi} A_{mn}^{jk} e^{i(m-k)\phi}\Big[I_{L1} + (-1)^{j+n-m+k} I_{L2}\Big]$$
$$I_{L1} = \int_0^\infty d\lambda \lambda^{j+n} K_{m-k}(\lambda\rho) e^{i\lambda Z}\Omega(i\lambda) \tag{34}$$
$$I_{L2} = \int_0^\infty d\lambda \lambda^{j+n} K_{m-k}(\lambda\rho) e^{-i\lambda Z}\Omega(-i\lambda)$$

and

$$\tilde{\Lambda}_U(\mathbf{r},\mathbf{r}';n,m,j,k) = \frac{i^{3j+n-|m-k|}}{\pi} A_{mn}^{jk} e^{i(m-k)\phi}\Big[I_{U1} + (-1)^{j+n-m+k} I_{U2}\Big]$$
$$I_{U1} = \int_0^\infty d\lambda \lambda^{j+n} K_{m-k}(\lambda\rho) e^{i\lambda Z}\Omega(-i\lambda) \tag{35}$$
$$I_{U2} = \int_0^\infty d\lambda \lambda^{j+n} K_{m-k}(\lambda\rho) e^{-i\lambda Z}\Omega(i\lambda).$$

The weight function $\Omega(\lambda)$ may have poles on the complex λ plane. This issue is discussed in Section 4.

3.3. Special Case: Source and Observation Points Are above Dielectric Interface

In [15] and [16], we have treated the special case of conductors above a stratified medium. The O2L translators were computed by summing a finite number of real images. Such an approach becomes intractable when there are more than three or four dielectric layers. A more generalized method is to numerically integrate Equation (32) or (34). The O2L translator for this problem has the form

$$\tilde{\alpha}_{nm}^{jk}(\mathbf{r},\mathbf{r}') = \alpha_{nm}^{jk}(\mathbf{r},\mathbf{r}') + \tilde{\Lambda}_L(\mathbf{r},\mathbf{r}';n,m,j,k) \tag{36}$$

where the $\Omega(\lambda)$ function for the image term is

$$\Omega_L(\lambda) = (-1)^{n+m}\tilde{R}_{12}(\lambda). \tag{37}$$

The difference between the z-coordinates of the first image cube center and the observation cube center is

$$Z_L = 2d_1 - z' - z. \tag{38}$$

While solving for Equation (36), we make an observation that, although irrelevant in this special geometric configuration,

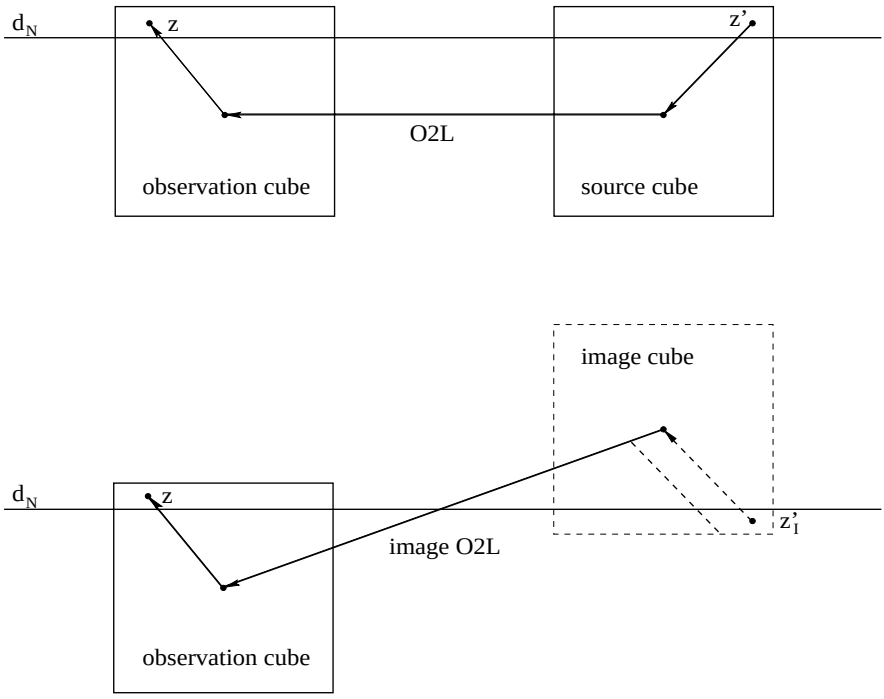

Figure 4. The locations of the first set of images of a source point in a stratified medium. The observation point is also in the region bounded by d_{U-1} and d_L.

integrals (34) and (35) are very important in developing the stratified medium FMM with conductors embedded in the dielectric layers. In Figure 4, the centers of the source and observation cubes are both below the dielectric interface. The consequence is that the center of the first image cube is above the dielectric interface. When this is the case, Equation (32) is invalid, and Equation (34) must be used to compute the image O2L multipole translator. As an example, we calculated $\tilde{\Lambda}_L(\mathbf{r}, \mathbf{r}'; n, m, j, k)$ as a function of θ while fixing all other parameters for the simple case of a microstrip substrate. The source cube center is at a fixed distance, $r = 1.5$, away from the observation cube center, which is at the origin. The azimuthal angle ϕ is fixed, while the zenith angle sweeps from 0 to 180°. Since the locations of the images can be determined without difficulty, we have summed the first 500 images and use this value as reference. In Figure 5, Equation (32) is clearly correct for $0 \leq \theta \leq 80°$. For $80° < \theta < 100°$, $z \simeq 0$, so Equation (32) cannot be numerically integrated. When $100° \leq \theta \leq 180°$, the integral

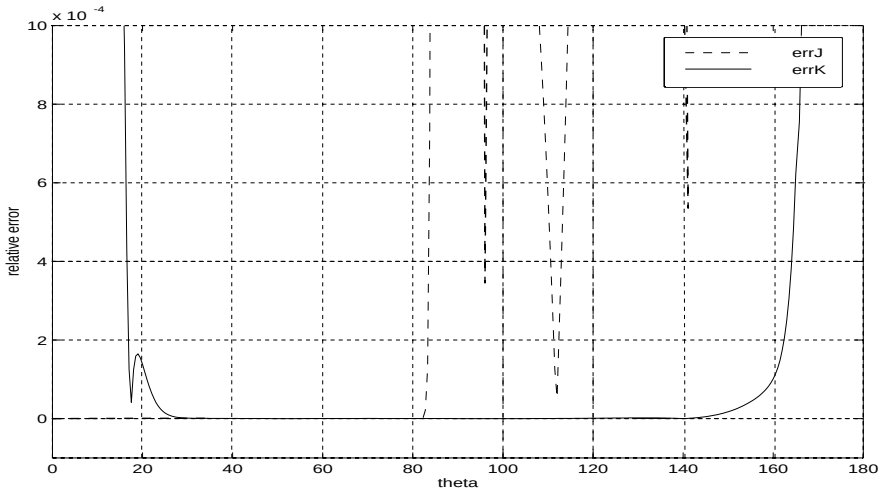

Figure 5. The absolute errors of numerically integrating Equations (3) and (4). The distance $r = 1.5$ and the azimuthal angle $\phi = 72°$. The order of outgoing multipole expansion is $n = 3,\ m = -1$, and the order of local multipole expansion is $j = 1,\ k = 0$.

in Equation (32) should converge well; however, the equation itself is invalid. The source of this error stems from the representation of the spherical harmonics as an integral of Bessel functions. In Equation (3), $Y_{n,m}(\theta, \phi)/r^{n+1}$ has different representations when $z \geq 0$ or $z \leq 0$. Therefore, Equation (34) must be used to compute the image O2L multipole translator when the centers of the source and field cubes are below a dielectric interface. For $140° \leq \theta \leq 180°$, the integrals in Equation (34) converge slowly. Fortunately, the zenith angle in image O2L multipole translator computation never exceeds 130°.

3.4. General Case: Source and Observation Points Are Embedded in a Multilayer Medium

The most general case in working with a stratified medium is that the conductors are embedded in the dielectric layers. In this general case, there are four sets of images instead of one described in the previous section. Similar to the calculation of the stratified medium Green's function, the general case can be separated into three subcases.

The first subcase we will consider is when the source and the observation cubes are in the same dielectric layer in a multilayer

medium. The O2L multipole translator can be written as

$$\begin{aligned}\tilde{\alpha}_{nm}^{jk}(\mathbf{r},\mathbf{r}') &= \alpha_{nm}^{jk}(\mathbf{r},\mathbf{r}')+\tilde{\Lambda}_{LL}^{MM}(\mathbf{r},\mathbf{r}';n,m,j,k)+\tilde{\Lambda}_{LU}^{MM}(\mathbf{r},\mathbf{r}';n,m,j,k)\\ &\quad+\tilde{\Lambda}_{UL}^{MM}(\mathbf{r},\mathbf{r}';n,m,j,k)+\tilde{\Lambda}_{UU}^{MM}(\mathbf{r},\mathbf{r}';n,m,j,k). \qquad (39)\end{aligned}$$

In Equation (39), $\alpha_{nm}^{jk}(\mathbf{r})$ is the free-space O2L translator given by Equation (29), and the weighting functions for the four image terms are

$$\Omega_{LL}^{MM}(\lambda) = \frac{\tilde{R}_{M,M+1}(\lambda)\tilde{R}_{M,M-1}(\lambda)}{1-\tilde{R}_{M,M+1}(\lambda)\tilde{R}_{M,M-1}(\lambda)e^{-\lambda 2t_M}} \qquad (40)$$

$$\Omega_{LU}^{MM}(\lambda) = \frac{(-1)^{n+m}\tilde{R}_{M,M+1}(\lambda)}{1-\tilde{R}_{M,M+1}(\lambda)\tilde{R}_{M,M-1}(\lambda)e^{-\lambda 2t_M}} \qquad (41)$$

$$\Omega_{UL}^{MM}(\lambda) = \frac{(-1)^{n+m}\tilde{R}_{M,M-1}(\lambda)}{1-\tilde{R}_{M,M+1}(\lambda)\tilde{R}_{M,M-1}(\lambda)e^{-\lambda 2t_M}} \qquad (42)$$

$$\Omega_{UU}^{MM}(\lambda) = \frac{\tilde{R}_{M,M+1}(\lambda)\tilde{R}_{M,M-1}(\lambda)}{1-\tilde{R}_{M,M+1}(\lambda)\tilde{R}_{M,M-1}(\lambda)e^{-\lambda 2t_M}}. \qquad (43)$$

The differences between the z-coordinates of the first set of image cube centers and the observation cube center are in Equation (15).

Next, we consider the case when the source cube of dielectric layer M is above the observation cube of dielectric layer N. The O2L multipole translator can be written as

$$\begin{aligned}\tilde{\alpha}_{nm}^{jk}(\mathbf{r},\mathbf{r}') &= \tilde{\Lambda}_{LL}^{MN}(\mathbf{r},\mathbf{r}';n,m,j,k)+\tilde{\Lambda}_{LU}^{MN}(\mathbf{r},\mathbf{r}';n,m,j,k)\\ &\quad+\tilde{\Lambda}_{UL}^{MN}(\mathbf{r},\mathbf{r}';n,m,j,k)+\tilde{\Lambda}_{UU}^{MN}(\mathbf{r},\mathbf{r}';n,m,j,k).\end{aligned} \qquad (44)$$

In Equation (44), the weighting functions for the four image terms are

$$\Omega_{LL}^{MN}(\lambda) = \frac{\tilde{T}_{M,N}^{-}(\lambda)\tilde{R}_{N,N+1}(\lambda)\tilde{R}_{M,M-1}(\lambda)}{1-\tilde{R}_{M,M+1}(\lambda)\tilde{R}_{M,M-1}(\lambda)e^{-\lambda 2t_M}} \qquad (45)$$

$$\Omega_{LU}^{MN}(\lambda) = \frac{(-1)^{n+m}\tilde{T}_{M,N}^{-}(\lambda)\tilde{R}_{N,N+1}(\lambda)}{1-\tilde{R}_{M,M+1}(\lambda)\tilde{R}_{M,M-1}(\lambda)e^{-\lambda 2t_M}} \qquad (46)$$

$$\Omega_{UL}^{MN}(\lambda) = \frac{\tilde{T}_{M,N}^{-}(\lambda)}{1-\tilde{R}_{M,M+1}(\lambda)\tilde{R}_{M,M-1}(\lambda)e^{-\lambda 2t_M}} \qquad (47)$$

$$\Omega_{UU}^{MN}(\lambda) = \frac{(-1)^{n+m}\tilde{T}_{M,N}^{-}(\lambda)\tilde{R}_{M,M-1}(\lambda)}{1-\tilde{R}_{M,M+1}(\lambda)\tilde{R}_{M,M-1}(\lambda)e^{-\lambda 2t_M}}. \qquad (48)$$

The differences between the z-coordinates of the first set of image cube centers and the observation cube center are in Equation (21).

Finally, for the case when the source cube of dielectric layer M is below the observation cube of dielectric layer N, the O2L multipole translator can be written as

$$\begin{aligned}\tilde{\alpha}_{nm}^{jk}(\mathbf{r},\mathbf{r}') = \tilde{\Lambda}_{LL}^{NM}(\mathbf{r},\mathbf{r}';n,m,j,k) + \tilde{\Lambda}_{LU}^{NM}(\mathbf{r},\mathbf{r}';n,m,j,k) \\ + \tilde{\Lambda}_{UL}^{NM}(\mathbf{r},\mathbf{r}';n,m,j,k) + \tilde{\Lambda}_{UU}^{NM}(\mathbf{r},\mathbf{r}';n,m,j,k).\end{aligned} \tag{49}$$

In Equation (49), the weighting functions for the four image terms are

$$\Omega_{LL}^{NM}(\lambda) = \frac{(-1)^{n+m}\tilde{T}_{M,N}^{+}(\lambda)\tilde{R}_{M,M+1}(\lambda)}{1-\tilde{R}_{M,M+1}(\lambda)\tilde{R}_{M,M-1}(\lambda)e^{-\lambda 2t_M}} \tag{50}$$

$$\Omega_{LU}^{NM}(\lambda) = \frac{\tilde{T}_{M,N}^{+}(\lambda)}{1-\tilde{R}_{M,M+1}(\lambda)\tilde{R}_{M,M-1}(\lambda)e^{-\lambda 2t_M}} \tag{51}$$

$$\Omega_{UL}^{NM}(\lambda) = \frac{(-1)^{n+m}\tilde{T}_{M,N}^{+}(\lambda)\tilde{R}_{N,N-1}(\lambda)}{1-\tilde{R}_{M,M+1}(\lambda)\tilde{R}_{M,M-1}(\lambda)e^{-\lambda 2t_M}} \tag{52}$$

$$\Omega_{UU}^{NM}(\lambda) = \frac{\tilde{T}_{M,N}^{+}(\lambda)\tilde{R}_{N,N-1}(\lambda)\tilde{R}_{M,M+1}(\lambda)}{1-\tilde{R}_{M,M+1}(\lambda)\tilde{R}_{M,M-1}(\lambda)e^{-\lambda 2t_M}}. \tag{53}$$

The differences between the z-coordinates of the first set of image cube centers and the observation cube center are in Equation (27).

To verify Equations (39), (44), and (49), we have reproduced in Tables 4 and 5 the sample points in Tables 1 and 3 by the indirect route of first calculating the outgoing multipole expansion, then performing the O2L multipole translation using the $\tilde{\alpha}_{nm}^{jk}(\mathbf{r},\mathbf{r}')$ translators, and finally evaluating the local multipole expansion.

4. SINGULARITIES IN THE INTEGRALS

In the multilayer Green's function and the image O2L multipole translators, there are singularities from the generalized reflection and transmission coefficients and the weighting functions associated with each set of images. These poles may interfere with numerical integrations and contour deformations.

The integral representation of the monopole $1/r$ in Equation (1) can be thought of as the degenerate case of the Sommerfeld identity [19]

$$\frac{e^{ik_0 r}}{r} = i\int_0^\infty dk_\rho \frac{k_\rho}{k_z} J_0(k_\rho\rho)e^{ik_z|z|} \tag{54}$$

Table 4. Reproduction of Table 1 using the indirect route of first calculating multipole expansion, then performing the O2L multipole translation, and finally evaluating the local multipole expansion. In all cases, it is assumed that $z' = z = 0$.

	$\epsilon_{r2} = 9.80$ $\epsilon_{r3} = 2.55$ $h_1 = 1.0\,\text{mm}$ $h_2 = 1.0\,\text{mm}$		$\epsilon_{r2} = 2.55$ $\epsilon_{r3} = 9.80$ $h_1 = 1.0\,\text{mm}$ $h_2 = 1.0\,\text{mm}$	
ρ (mm)	direct	FMM	direct	FMM
0.1	1622.29	1622.43	1522.03	1522.21
0.6	270.20	270.20	177.00	177.00
1.1	142.91	142.91	63.23	63.23
1.6	91.90	91.91	27.53	27.55
2.1	63.52	63.53	13.16	13.17
3.1	33.31	33.30	3.59	3.58

Table 5. Reproduction of Table 3 using the indirect route of first calculating multipole expansion, then performing the O2L multipole translation, and finally evaluating the local multipole expansion ($\epsilon_{r2} = 9.8,\ \epsilon_{r3} = 2.55$).

	$z' = 1.1\,\text{mm}$	$z = -0.1\,\text{mm}$	$z' = -0.1\,\text{mm}$	$z = 1.1\,\text{mm}$
ρ (mm)	direct	FMM	direct	FMM
0.1	177.64	177.64	177.64	177.64
0.6	153.28	153.28	153.28	153.28
1.1	116.20	116.20	116.20	116.20
1.6	84.63	84.63	84.63	84.63
2.1	61.56	61.56	61.56	61.56
3.1	33.64	33.62	33.64	33.62

when $k_0 \to 0$. Since $k_z = (k_0^2 - k_\rho^2)^{1/2}$, Equation (54) is reduced to Equation (1) via the following relations:

$$\lambda \equiv \sqrt{k_\rho^2}, \tag{55}$$

$$k_z = i\lambda. \tag{56}$$

To ensure the radiation condition, $\Re e\{k_z\} > 0$ and $\Im m\{k_z\} > 0$. So on the top Riemann sheet defined by $\Im m\{k_z\} = 0$ branch cuts, $\Im m\{\lambda\} > 0$.

Figure 6 is a graphical view of the top Riemann sheet defined by $\Im m\{k_z\} = 0$ for the degenerate case of $k_0 \to 0$. The Sommerfeld integration path (SIP) is also shown in the figure. Equation (2) is arrived at by using Cauchy's theorem and Jordan's lemma to deform the SIP to a clockwise integration wrapping around the branch cut.

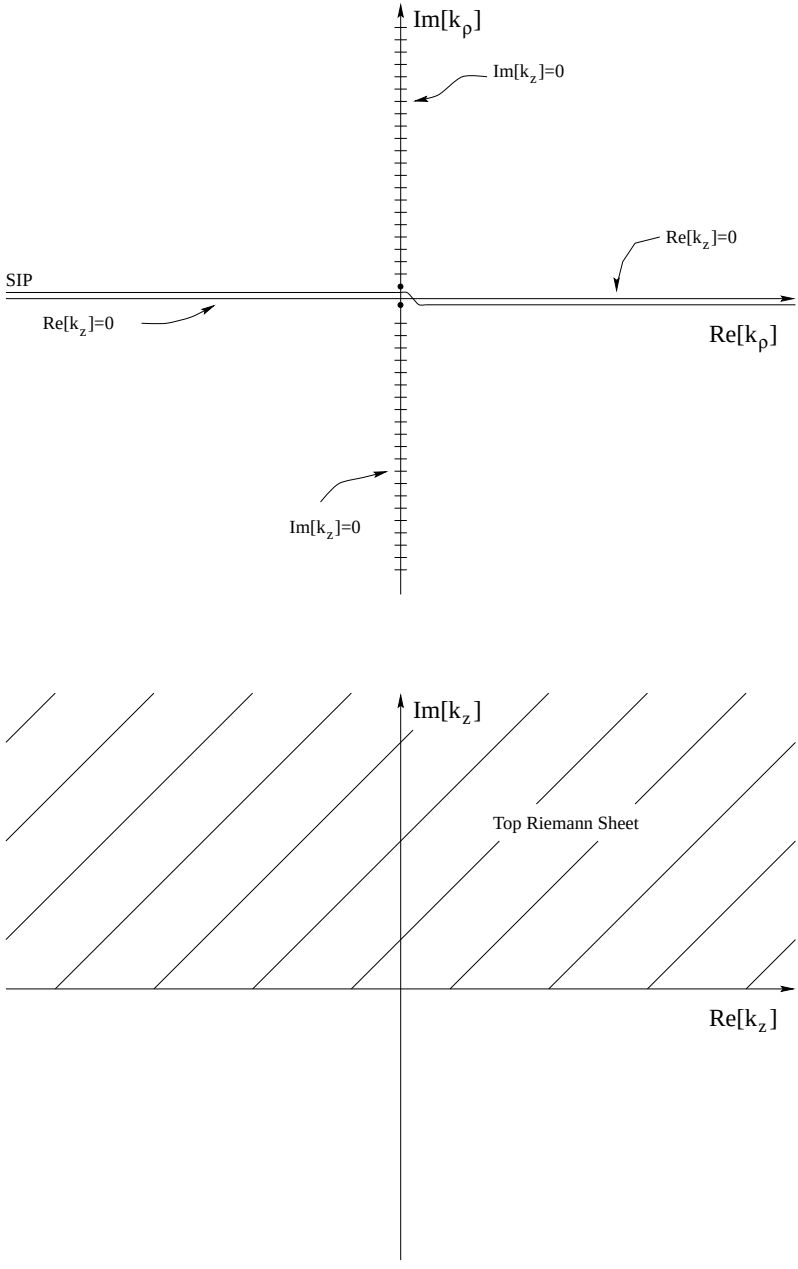

Figure 6. The top Riemann sheet defined by $\Im m\{k_z\} = 0$ for the degenerate case of $k_0 \to 0$.

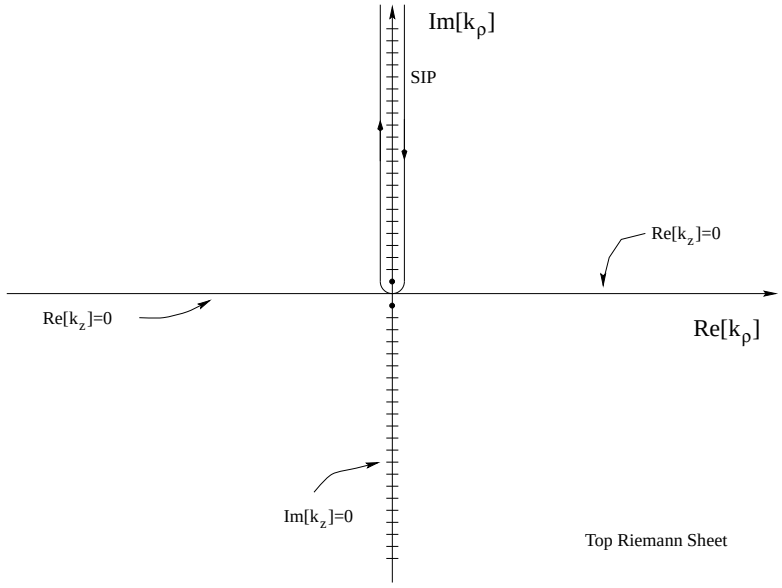

Figure 7. The deformed contour of integration wraps around the branch cut.

The deformed contour of integration is shown in Figure 7. This change of integration path is perfectly fine in the free-space case. In the presence of dielectric media, however, one must ascertain that no singularity exists on the top Riemann sheet and the real and imaginary axes.

4.1. Singularities in the Generalized Reflection and Transmission Coefficients

The generalized reflection and transmission coefficients have poles when the denominators in Equations (A1), (A2), (A5), and (A6) become zero. The poles in these coefficients are on the bottom Riemann sheet and off the real and imaginary axes, and therefore do not interfere with numerical integration or integration contour deformation.

The denominators of the generalized reflection and transmission coefficients have the form

$$D_r = 1 + r\tilde{R}(\lambda)e^{i\lambda t} \tag{57}$$

where r is a reflection coefficient, $\tilde{R}(\lambda)$ is a generalized reflection coefficient, and t is a thickness. For lossless dielectrics, the reflection

coefficients $r_{i,i+1}$ and $r_{i+1,i}$, given in Equations (A7) and (A8), have magnitudes less than 1. They have magnitudes equal to 1 if and only if one of the media is a ground plane. Hence, it can easily be shown by induction that the magnitudes of $\tilde{R}_{i,i+1}(\lambda)$ and $\tilde{R}_{i+1,i}(\lambda)$ are at most 1 on the top Riemann sheet. Furthermore, the magnitude of $\tilde{R}_{i+1,i}(\lambda)$ is 1 if and only if the stratified medium is bounded below by a ground plane; the magnitude of $\tilde{R}_{i+1,i}(\lambda)$ is 1 if and only if the stratified medium is bounded above by a ground plane. So the denominators in Equations (A1), (A2), (A5), and (A6) are never zero on the top Riemann sheet. These denominators can be zero only if the real part of λ is negative. Therefore, the poles in the reflection and transmission coefficients are not on the top Riemman sheet.

4.2. Weighting Functions

In the previous section, it was shown that the poles of the reflection and transmission coefficients are off the real and imaginary axes, and are on the bottom Riemann sheet. The denominators of the weighting functions have form

$$D_w = 1 - \tilde{R}_{i,i-1}(\lambda)\tilde{R}_{i,i+1}(\lambda)e^{i\lambda t}. \tag{58}$$

For a multilayered medium bounded by at most one ground plane, the magnitude of at least one of the generalized reflection coefficients is always less than 1. Hence, by the proof from the last section, none of the weighting functions has poles on the real or the imaginary axes. From the radiation condition, it is also true that the poles are on the bottom Riemann sheet. For the special class of layered media bounded above and below by two ground planes, however, the poles of the weighting functions are along the imaginary axis. Of these poles, the one at the origin is fixed, while the locations of the others are functions of the thicknesses of the dielectric layers. This case is currently being studied.

Figure 8 contains the contour plots of the integrand in Equation (7) for the simple case of a medium with two layers of dielectrics supported on the bottom by a ground plane. It is clear from the figure that the top Riemann sheet does not have poles for the integrands in Equation (7), so contour deformation is possible.

5. SMFMM FOR GENERAL 3D STRUCTURES

5.1. General Formulation

Our new stratified medium FMM (SMFMM) will solve for the a capacitance matrix of a complex conductor structure embedded in

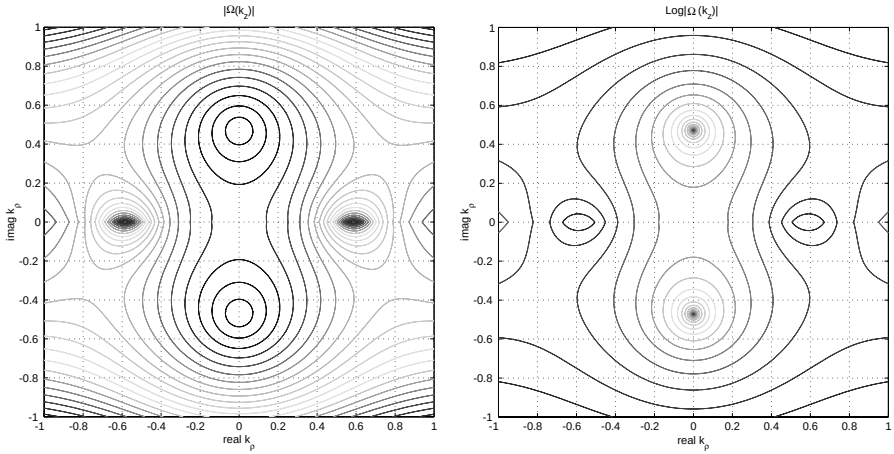

Figure 8. The top plot shows the absolute value of the integrand in Equation (7) over the complex k_ρ plane. The bottom plot is the logarithmic plot of the top one.

a dielectric substrate with an arbitrary number of layers. Figure 1 depicts one possible configuration.

The integral-equation method of calculating the capacitance matrix requires finding the charge distribution $\rho(\mathbf{r})$ on the surfaces of the conductors while the potentials on the conductors are fixed. Once the charge distribution is known, we can integrate over the surface of the conductors to compute the total charge present on each conductor. The elements of the capacitance matrix can then be found directly from the definition:

$$Q_n = \sum_{m=1}^{M} C_{nm} V_m. \tag{59}$$

In (59), M is the number of conductors, $n = 1, 2, \ldots, M$, Q_n is the total charge on conductor n, V_m is the voltage on conductor m, and C_{nm} is the nmth element of the capacitance matrix. The charge distribution $\rho(\mathbf{r})$ is the solution to the integral equation

$$\Phi(\mathbf{r}) = \sum_{n=1}^{M} \int_{S_n} dS' \tilde{G}(\mathbf{r}, \mathbf{r}') \rho(\mathbf{r}') \quad \mathbf{r} \in S_m, \ m = 1, 2, \ldots, M. \tag{60}$$

In (60), Φ is the potential, S_n is the surface of the nth conductor, and $\tilde{G}(\mathbf{r}, \mathbf{r}')$ is the multilayer Green's function. There are several forms of

the multilayer Green's function in the literature, notably in [1–7]. We derived a new form based on the integral representation of the spherical harmonics and the generalized reflection and transmission coefficients in the previous sections.

The surface of the conductors is discretized into N triangular patches using MOM. For simplicity, we assume $\rho = \rho_l$ is constant on each patch and use the point-matching method. The integral equation of (60) is discretized through MOM in the form of a matrix equation of unknown charge density $\boldsymbol{\rho}$:

$$\boldsymbol{\Psi} = \bar{\mathbf{M}} \cdot \boldsymbol{\rho}. \tag{61}$$

The cost of solving (61) using the iterative conjugate gradient method is $O(N^2)$ per iteration. Our SMFMM method can reduce this cost to $O(N)$.

5.2. Brief Overview of Multilevel Free-Space Fast Multipole Method

The outgoing multipole expansion of a group of N sources is defined as

$$\Phi(\mathbf{r}) = \sum_{n=0}^{\infty} \sum_{m=-n}^{n} \frac{M_{nm}}{r^{n+1}} Y_{nm}(\theta, \phi) \tag{62}$$

where M_{nm} are the outgoing multipole coefficients given by

$$M_{nm} = \sum_{i=1}^{N} q_i r_i' Y_{n_i - m}(\theta_i', \phi_i') \tag{63}$$

and $Y_{nm}(\theta, \phi)$ is the spherical harmonics.

In the free-space multilevel FMM, the sources are enclosed in a large cube. This cube is called the level 0 cube. The level 0 cube is divided into eight equally sized, level 1, child cubes. Each child cube is recursively subdivided into smaller cubes until none of the finest level cubes contains more than a fixed number of sources. The relationships between the cubes are stored in a tree structure.

An L-level free-space FMM is performed in the following two stages:

1. Aggregation stage:
   (a) For each occupied cube on level L, construct the outgoing multipole expansion of the sources within the cube about the cube's center.

(b) For each occupied cube on level $L-1$, construct the outgoing multipole expansion about the cube's center by translating the outgoing multipole expansions of its eight child cubes.
(c) Repeat the process for each of the coarser levels.

2. Disaggregation stage:
   (a) For each occupied cube on level 2, construct local multipole expansion about the cube's center by translating the outgoing multipole expansions of its interaction cubes.
   (b) For each occupied cube on level 3, construct local multipole expansion about the cube's center using the following two steps:
      - translating the parent cube's local expansion,
      - translating the outgoing multipole expansions of its interaction cubes.
   (c) Repeat the process for each of the finer levels until the local multipole expansions are constructed for each of the occupied cubes on level L.

To evaluate the potential at a field point within a cube on level L, we first calculate directly the contribution from sources within the given cube and in the nearest neighbors of the given cube, and then add the contribution from distant sources by evaluating the local multipole expansion

$$\Phi(\mathbf{r}') = \sum_{j=0}^{\infty} \sum_{k=-j}^{j} L_{jk}(r'_l) Y_{jk}(\theta'_l, \phi'_l). \tag{64}$$

5.3. Description of SMFMM

Our previous SMFMM in [15] and [16] was based on the observation that, with the correct choice of the image cube, the image outgoing multipole expansion is a scalar multiple of the free-space outgoing multipole expansion. Following this idea, we developed an efficient FMM for conductors above the a stratified medium where the effect of the dielectric medium is incorporated by translating the image outgoing multipole expansions to local multipole expansion in the disaggregation stage of the FMM. This algorithm, unfortunately, cannot be used to deal with conductors embedded in a dielectric medium because we only worked with one set of images. Furthermore, only the case of the source and field points in the same dielectric region is considered. In this section, we will describe a new SMFMM algorithm that can solve this more general capacitance extraction problem.

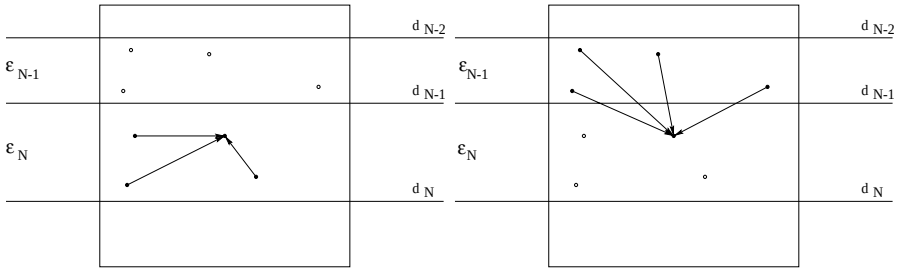

Figure 9. Multiple copies of a cube are needed if the cube straddles more than one layer. In the figures above, sources from upper and lower dielectric layers must form different outgoing multipole expansion.

5.3.1. Multiple Tree Structure

To have the ability to extract the capacitance matrix when the conductors are embedded in a stratified medium, we must first organize the sources to different tree structures. This need arises from the fact that the layered medium Green's function is specific to the dielectric regions of the source and field points. As a consequence, as shown in Figure 9, two different outgoing multipole expansions must be performed for the cube diagrammed: one for sources in region $N-1$ and the other for sources in region N.

In our new SMFMM, the number of tree structures is determined by the number of dielectric layers that are occupied by at least one source patch. To facilitate bookkeeping, all level-0 cubes coincide. All trees also have the same number of levels.

5.3.2. Buffer Zone for SMFMM

In SMFMM, cubes that straddle one or more dielectric interfaces may present a violation of the addition theorem. In Figure 10, the centers of the first image cube and the field cube are closer than the minimum 2.0 cube length needed to guarantee convergence, which can introduce larger than expected numerical errors.

The problem can be resolved by specifying a two-cube buffer in the $\pm z$-direction, the direction normal to dielectric interfaces (Figure 11).

In a multilevel implementation of the FMM, however, one more layer of buffer cubes leads to more cubes in the interaction list. Figure 12 shows an increase in the number of possible interaction cube locations for SMFMM. In a traditional FMM with a one-cube buffer, there are 316 possible interaction cube locations. In SMFMM, there are now 494 possible interaction cube locations.

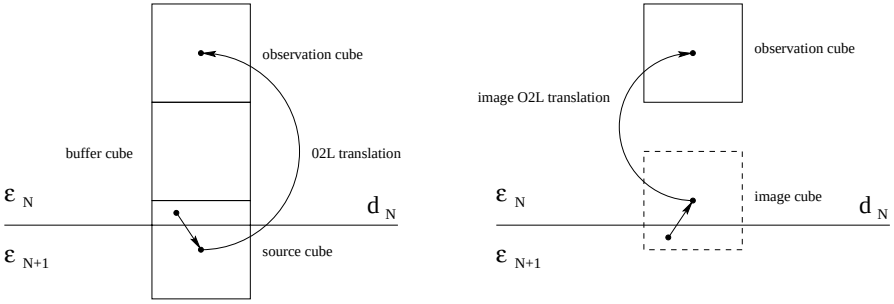

Figure 10. When a source cube straddles a dielectric interface, some of its image cubes may be closer to the observation cube than the cube itself. In this figure, the centers of the first image cube and the observation cube are clearly closer than the minimum 2 cube lengths needed to guarantee numerical accuracy.

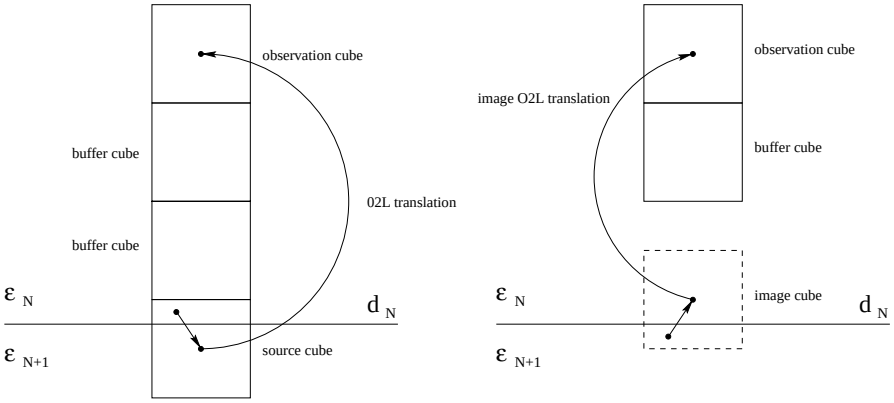

Figure 11. By specifying one more layer of buffer cubes in the $\pm z$-direction, the convergence is guaranteed because none of the image cubes is too close to the observation cube.

5.3.3. Intralayer O2L Translation

In general, there are three different types of O2L translations, depending on whether the source cube is in a dielectric layer above, the same as, or below the dielectric layer of the observation cube. The O2L translation is termed intralayer translation if the source and the observation cubes are of the same dielectric layer. Figure 13 shows the portion of SMFMM interaction cubes that need intralayer O2L translation.

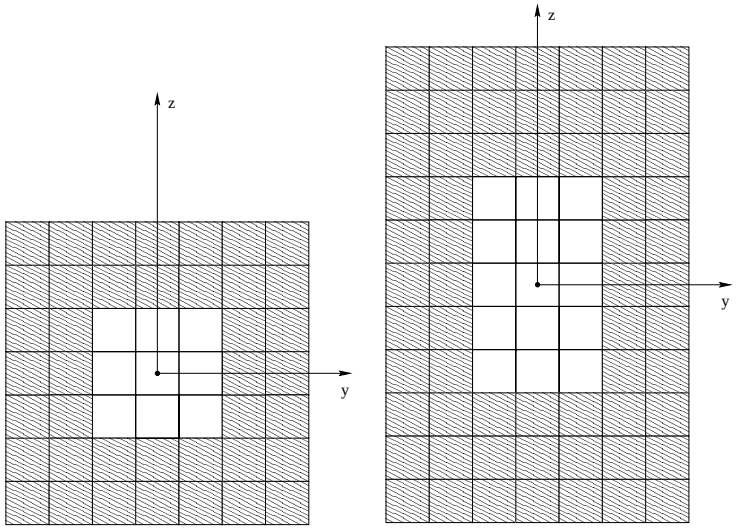

Figure 12. As a consequence of specifying one more layer of buffer cubes in the $\pm z$-direction there are more possible interaction cube locations in SMFMM. The figure on the left shows possible interaction cube locations for a traditional FMM, while the one on the right shows an increase in the number of possible interaction locations for SMFMM.

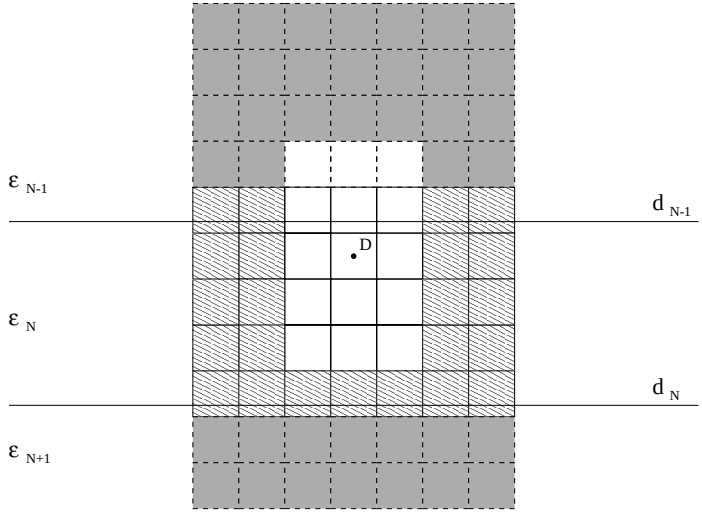

Figure 13. The lightly shaded interaction cubes require intralayer O2L multipole translation.

The intralayer O2L translation is governed by translator

$$\tilde{\alpha}_{nm}^{jk}(\mathbf{r},\mathbf{r}')_{MM} = \alpha_{nm}^{jk}(\mathbf{r},\mathbf{r}') + \tilde{\Lambda}_{LL}^{MM}(\mathbf{r},\mathbf{r}';n,m,j,k) + \tilde{\Lambda}_{LU}^{MM}(\mathbf{r},\mathbf{r}';n,m,j,k) + \tilde{\Lambda}_{UL}^{MM}(\mathbf{r},\mathbf{r}';n,m,j,k) + \tilde{\Lambda}_{UU}^{MM}(\mathbf{r},\mathbf{r}';n,m,j,k) \quad (65)$$

For the four image terms in (65), M is the dielectric layer number, the subscripts specify the set of images, and the superscript MM indicates that the source and observation cubes are in the same dielectric layer M. The computation of the five terms on the right-hand side of (65) is discussed in Section 3. A graphical representation of them is in Figure 14.

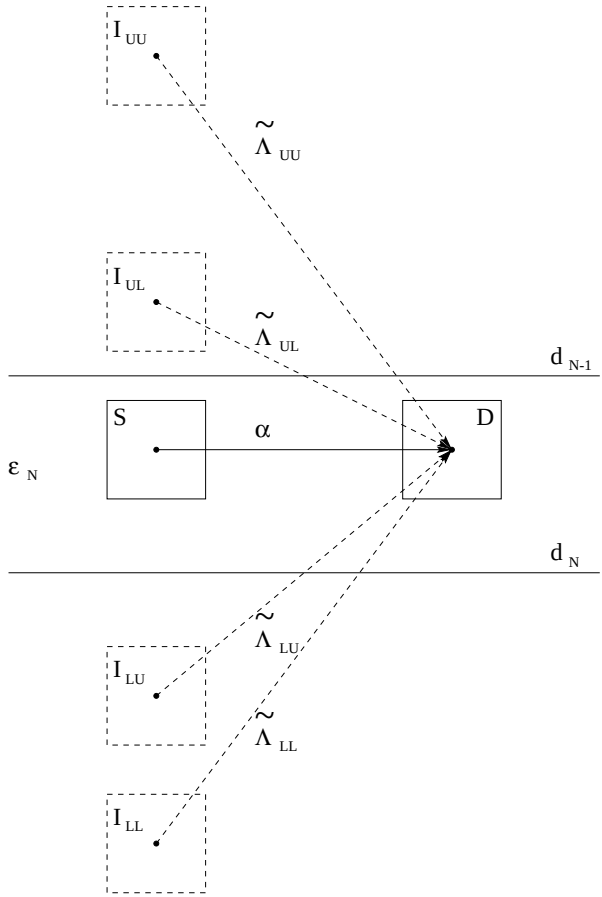

Figure 14. A graphical representation of the five terms on the right-hand side of (65).

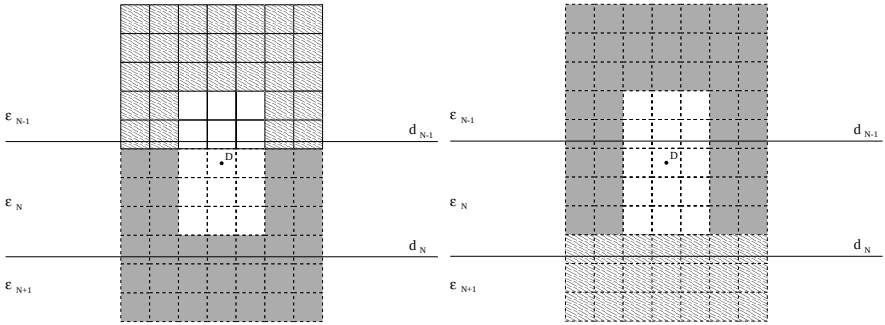

Figure 15. The lightly shaded interaction cubes require intralayer O2L multipole translation.

5.3.4. Interlayer O2L Translation

In most cases, an observation cube has interaction cubes that contain outgoing multipole expansions of sources in dielectric layers above or below its own dielectric layer. As depicted in Figure 15, the observation cube D, which is in dielectric layer N, has interaction cubes from dielectric layer $N-1$ as well as dielectric layer $N+1$. Notice that the two layers of cubes that straddle the dielectric interfaces d_{N-1} and d_N are also considered in Figure 13. This is because multiple copies of these cubes are created to store outgoing multipole expansions of sources in different dielectric layers.

Assume that the source cube is in dielectric layer M and the observation cube is in dielectric layer N. Let superscript NM designate the case of dielectric layer N above dielectric layer M, and MN the case of dielectric layer N below dielectric layer M. The interlayer O2L translators are given by

$$\begin{aligned}\tilde{\alpha}_{nm}^{jk}(\mathbf{r},\mathbf{r}')_{NM} &= \tilde{\Lambda}_{LL}^{NM}(\mathbf{r},\mathbf{r}';n,m,j,k)+\tilde{\Lambda}_{LU}^{NM}(\mathbf{r},\mathbf{r}';n,m,j,k)\\ &\quad+\tilde{\Lambda}_{UL}^{NM}(\mathbf{r},\mathbf{r}';n,m,j,k)+\tilde{\Lambda}_{UU}^{NM}(\mathbf{r},\mathbf{r}';n,m,j,k) \quad (66)\\ \tilde{\alpha}_{nm}^{jk}(\mathbf{r},\mathbf{r}')_{MN} &= \tilde{\Lambda}_{LL}^{MN}(\mathbf{r},\mathbf{r}';n,m,j,k)+\tilde{\Lambda}_{LU}^{MN}(\mathbf{r},\mathbf{r}';n,m,j,k)\\ &\quad+\tilde{\Lambda}_{UL}^{MN}(\mathbf{r},\mathbf{r}';n,m,j,k)+\tilde{\Lambda}_{UU}^{MN}(\mathbf{r},\mathbf{r}';n,m,j,k). \quad (67)\end{aligned}$$

Discussion of the computation of the terms on the right-hand side of (66) and (67) is given in Section 3. The two plots in Figure 16 are pictorial depiction of these terms.

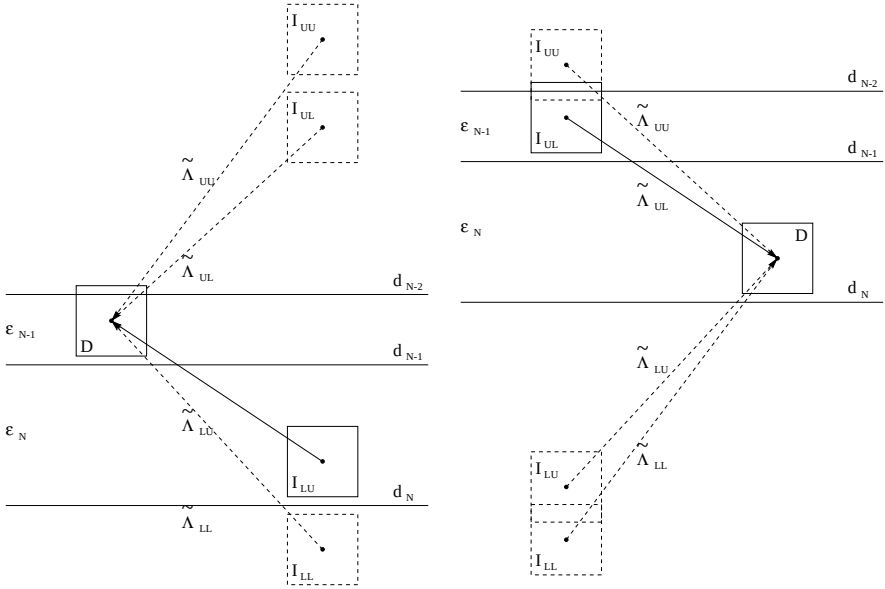

Figure 16. A graphical representation of the four terms on the right-hand side of Equations (66) and (67).

5.3.5. Details of the SMFMM

In Sections 5.3.1–5.3.4, we discussed some concepts and concerns in the new SMFMM. In this section, we will outline the details of the algorithm.

1. Setup stage:
   (a) Sort through all conductor patches to determine the number of required trees.
   (b) Ignore the stratified medium to form the level-0 cubes for all trees.
   (c) Determine the number of FMM levels, L.
   (d) For each tree, find the intralayer and interlayer interaction lists.
   (e) For each tree, determine and compute all necessary intralayer and interlayer O2L translators.
   (f) Determine and fill the sparse direct matrix.
2. Aggregation stage:
   (a) For each tree, construct all level-L outgoing multipole expansions.

(b) For each tree, construct all coarser level outgoing multipole expansions using the free-space outgoing-to-outgoing (O2O) translators.

3. Disaggregation stage:
   (a) For each occupied cube on level 2, construct the local multipole expansion by
      - translating the outgoing multipole expansions of the cubes in the intralayer interaction list, and
      - translating the outgoing multipole expansions of the cubes in the interlayer interaction list.
   (b) For each occupied cube on level 3, construct the local multipole expansion by
      - translating the parent cube's local expansion using the free-space local-to-local (L2L) multipole translators,
      - translating the outgoing multipole expansions of the cubes in the intralayer interaction list, and
      - translating the outgoing multipole expansions of the cubes in the interlayer interaction list.
   (c) Repeat the process for each of the finer levels until the local multipole expansions are constructed for each of the occupied cubes on level L.
4. Evaluation stage:
   (a) Evaluate contributions from nearby sources using the sparse direct matrix.
   (b) Evaluate contributions from distant sources using the local multipole expansions.

5.4. Numerical Results

The accuracies of our multilayer Green's function and SMFMM are checked by comparison to the well-known results in [7] and [3].

We first tested SMFMM on Example 2 of [3]. This problem consists of two microstrip lines with rectangular cross-section and one with circular cross-section. All lines in [3] are 2 m in length. Figure 17 is a cross-sectional view of the geometry. In [3], the circular conductor is modeled by using 80 triangular patches. The rectangular conductors are each modeled utilizing 40 triangular patches. Furthermore, the dielectric layers are 2×2 m and are each modeled by 32 triangular patches. In our calculation, each of the rectangular microstrip lines is modeled by 68 triangular patches, and the circular line is modeled by 200 triangular patches. Our dielectric interfaces and the ground plane are infinite in the xy-plane.

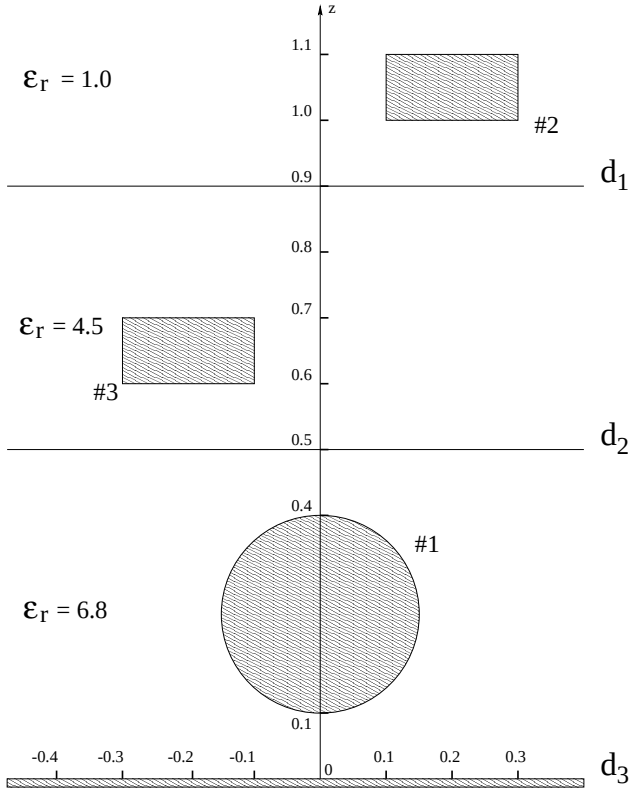

Figure 17. A cross-sectional view of the geometry in Example 2 of [3]. The conductors are 2 m long.

The results of our calculation are presented in Table 6. In the table, the first column contains the reference capacitance matrix from [3]. The second column contains the capacitance matrix calculated with 336 unknowns. These numbers of unknowns are inadequate to capture the corner and edge effects. In the third column, we re-calculated the capacitance matrix using 26,154 unknowns. The units in Table 6 are pF/m.

The accuracy of our method is further verified with 2-D data presented in [7]. The geometry of this problem is shown in Figure 18. In our calculation, the conductors are 2000 μm in length, which is much larger than the cross-sectional dimensions. Each of the three microstrip lines is modeled using 9,808 triangular patches. The units in Table 7 are pF/m.

Table 6. Comparison of computed capacitances with data published in [3]. Conductor 1 is the circular line, conductor 2 is the right-hand rectangular line, and conductor 3 is the left-hand rectangular line.

3-D analysis in [3]			SMFMM (336 unknowns)			SMFMM (26,154 unknowns)		
398.4	−66.6	−6.7	394.6	−68.3	−6.7	428.9	−73.4	−7.2
−69.7	139.9	−12.2	−68.2	141.7	−12.0	−73.4	146.9	−12.5
−7.6	−12.9	38.2	−6.7	−12.0	38.3	−7.2	−12.5	39.5

Table 7. Comparison of computed capacitances with 2-D data published in [7]. In our 3-D simulation, the conductors are 2000 μm long, and are modeled with a total of 29,436 triangular patches.

2-D analysis in [7]			SMFMM (29,436 unknowns)		
141.4	−21.5	−1.0	157.9	−21.5	−0.8
−21.5	94.0	−17.8	−21.5	102.6	−17.6
−0.9	−17.8	87.5	−0.8	−17.6	97.5

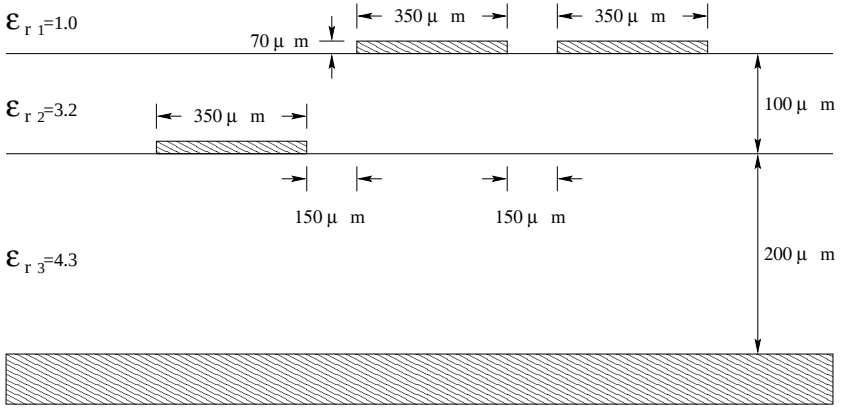

Figure 18. A cross-sectional view of the geometry in [7]. The conductors are 2000 μm long.

To test SMFMM on a more complex structure, we regenerated the geometry with two signal lines passing through two conducting planes, which was presented in [20]. In [20], this structure is in free space, and is modeled using 6,185 panels. In our calculation, the structure is embedded in four layers of dielectrics, and is modeled using 128,600 triangular patches. Figure 19 shows a coarser 3-D rendering of the

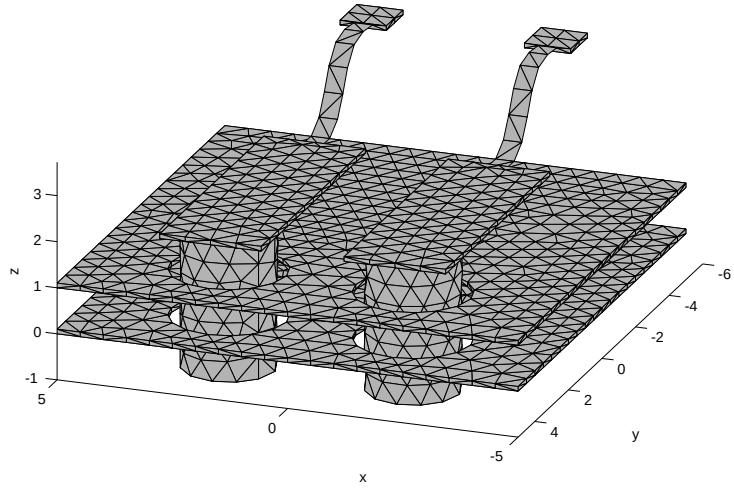

Figure 19. The 3-D rendering of the conductor geometry with two signal lines passing though conducting planes. The structure in this figure contains 4,580 triangular patches.

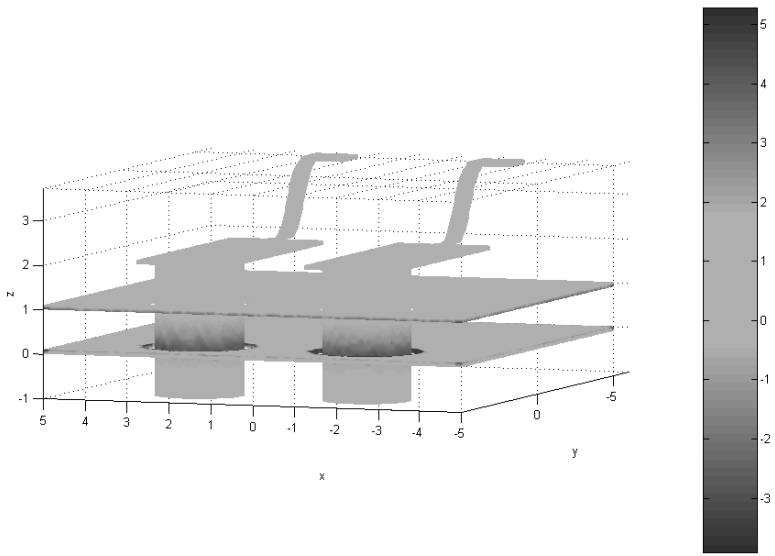

Figure 20. The conductor structure [20] presented in Figure 19 is solved using a finer mesh with 128,600 triangular patches. The charge densities on the conductors are plotted. In this plot, the lower conductor plate is set to 1 V while the other plate and the two signal lines are set to 0 V.

conductor structure using 4,580 patches. The coarser mesh is necessary in order to see the individual patches. The calculated surface charge densities of the conductors, for the case when the lower conductor plate is set to 1 V and the all other conductors to 0 V, are plotted in Figure 20.

6. CONCLUSION

In this paper, we have developed the integral representations of the stratified medium Green's function and the stratified medium O2L multipole translators using the integral representation of the spherical harmonics. These formulae are used to develop a new SMFMM algorithm for extracting the capacitance matrix of a complex conductor structure embedded in a stratified medium. In this SMFMM, the image outgoing multipole expansions are used to efficiently account for the presence of multiple layers of dielectrics, and therefore it has computational complexity and memory requirement of $O(N)$.

ACKNOWLEDGMENT

This work is supported by Air Force Office of Scientific Research under MURI grant F49620-96-1-0025, Raytheon Company, Semiconductor Research Corporation, and Texas Instruments.

APPENDIX A.

The generalized reflection coefficients are

$$\tilde{R}_{i,i+1}(\lambda) = \frac{r_{i,i+1} + \tilde{R}_{i+1,i+2}(\lambda)e^{i\lambda 2t_{i+1}}}{1 + r_{i,i+1}\tilde{R}_{i+1,i+2}(\lambda)e^{i\lambda 2t_{i+1}}} \tag{A1}$$

$$\tilde{R}_{i+1,i}(\lambda) = \frac{r_{i+1,i} + \tilde{R}_{i,i-1}(\lambda)e^{i\lambda 2t_i}}{1 + r_{i,i+1}\tilde{R}_{i,i-1}(\lambda)e^{i\lambda 2t_i}}. \tag{A2}$$

The generalized transmission coefficients are

$$\tilde{T}^{-}_{M,N}(\lambda) = \prod_{i=M}^{N-1} \tilde{T}_{i,i+1}(\lambda) \tag{A3}$$

$$\tilde{T}^{+}_{M,N}(\lambda) = \prod_{i=N}^{M-1} \tilde{T}_{i+1,i}(\lambda) \tag{A4}$$

$$\tilde{T}_{i,i+1}(\lambda) = \frac{T_{i,i+1}}{1 - r_{i+1,i}\tilde{R}_{i+1,i+2}(\lambda)e^{i\lambda 2t_{i+1}}} \tag{A5}$$

$$\tilde{T}_{i+1,i}(\lambda) = \frac{T_{i+1,i}}{1 - r_{i,i+1}\tilde{R}_{i,i-1}(\lambda)e^{i\lambda 2t_i}}. \tag{A6}$$

The reflection and transmission coefficients at a dielectric interface are

$$r_{i,i+1} = \frac{\epsilon_i - \epsilon_{i+1}}{\epsilon_i + \epsilon_{i+1}} \tag{A7}$$

$$r_{i+1,i} = \frac{\epsilon_{i+1} - \epsilon_i}{\epsilon_{i+1} + \epsilon_i} \tag{A8}$$

$$t_{i,i+1} = \frac{2\epsilon_i}{\epsilon_i + \epsilon_{i+1}} \tag{A9}$$

$$t_{i+1,i} = \frac{2\epsilon_{i+1}}{\epsilon_{i+1} + \epsilon_i}. \tag{A10}$$

REFERENCES

1. Weeks, W. T., "Calculation of coefficients of capacitance of multiconductor transmission lines in the presence of a dielectric interface," *IEEE Trans. Microwave Theory Tech.*, Vol. MTT-18, 35–43, Jan. 1970.
2. Wei, C., R. F. Harrington, J. R. Mautz, and T. K. Sarkar, "Multiconductor transmission lines in multilayered dielectric media," *IEEE Trans. Microwave Theory Tech.*, Vol. MTT-32, 439–450, Apr. 1984.
3. Rao, S. M., T. K. Sarkar, and R. F. Harrington, "The electrostatic field of conducting bodies in multiple dielectric media," *IEEE Trans. Microwave Theory Tech.*, Vol. 32, No. 11, 1441–1448, Nov. 1984.
4. Das, N. K. and D. M. Pozar, "A generalized spectral-domain Green's function for multilayer dielectric substrates with application to multilayer transmission lines," *IEEE Trans. Microwave Theory Tech.*, Vol. MTT-35, 326–335, Mar. 1987.
5. Delbare, W. and D. D. Zutter, "Space-domain Green's function approach to the capacitance calculation of multiconductor lines in multilayered dielectrics with improved surface charge modeling," *IEEE Trans. Microwave Theory Tech.*, Vol. 37, 1562–1568, Oct. 1989.
6. Zemanian, A. H., R. P. Tewarson, C. P. Ju, and J. F. Jen, "Three-dimensional capacitance computations for VLSI/ULSI

interconnections," *IEEE Trans. CAD*, Vol. CAD-8, 1319–1326, Dec. 1989.

7. Oh, K. S., D. Kuznetsov, and J. E. Schutt-Aine, "Capacitance computations in a multilayered dielectric medium using closed-form spatial Green's functions," *IEEE Trans. Microwave Theory Tech.*, Vol. 42, 1443–1453, Aug. 1994.
8. Harrington, R. F., *Field Computation by Moment Methods*, MacMillan, New York, 1968.
9. Greengard, L. and V. Rokhlin, "A fast algorithm for particle simulations," *J. Comp. Phys.*, Vol. 73, 325–348, 1987.
10. Greengard, L., *The Rapid Evaluation of Potential Fields in Particle Systems*, M.I.T. Press, Cambridge, MA, 1988.
11. Nabors, K. and J. White, "FastCap: A multipole accelerated 3-D capacitance extraction program," *IEEE Trans. Computer-Aided Design*, Vol. 10, 1447–1459, Nov. 1991.
12. Jandhyala, V., E. Michielssen, and R. Mittra, "Multipole-accelerated capacitance computation for 3-D structures in a stratified dielectric medium using a closed-form Green's function," *International J. of Microwave and Millimeter-Wave Computer-Aided Eng.*, Vol. 5, 68–78, May 1995.
13. Jandhyala, V., E. Michielssen, and R. Mittra, "Memory-efficient, adaptive algorithm for multipole-accelerated capacitance computation in a stratified dielectric medium," *International J. of Microwave and Millimeter-Wave Computer-Aided Eng.*, Vol. 6, 381–390, Nov. 1996.
14. Kapur, S. and D. E. Long, "Large-scale capacitance calculation," *Proc. Design Automation Conf. 2000*, 744–749, Piscataway, NJ, 2000.
15. Pan, Y. C. and W. C. Chew, "A hierarchical fast multipole method for stratified media," *Microwave and Optical Tech. Letters*, Vol. 37, No. 1, 13–17, Oct. 2000.
16. Pan, Y. C., W. C. Chew, and L. X. Wan, "A fast multipole method based calculation of the capacitance matrix for multiple conductors above stratified dielectric media," *IEEE Trans. Microwave Theory Tech.*, Vol. 39, No. 3, 480–490, March 2001.
17. Pan, Y. C. and W. C. Chew, "A generalized method for the computation of the outgoing-to-local multipole translators," *Proc. IEEE Int. Antennas Propagat. Symp. Dig.*, 802–805, Boston, MA, July 2001.
18. Chow, Y. L., J. J. Yang, and G. E. Howard, "Complex images for electrostatic field computation in multilayered media," *IEEE*

Trans. Microwave Theory Tech., Vol. 39, No. 7, 1120–1125, July 1991.

19. Chew, W. C., *Wave and Fields in Inhomogeneous Media*, Van Nostrand Reinhold, New York, 1990.
20. Nabors, K., S. Kim, and J. White, "Fast capacitance extraction of general three-dimensional structures," *IEEE Trans. Microwave Theory Tech.*, Vol. 40, 1496–1506, July 1992.